
An Investigation of Conformal Isometry Hypothesis for Grid Cells

Dehong Xu¹
xudehong1996@ucla.edu

Ruiqi Gao²
ruiqig@google.com

Wen-Hao Zhang³
Wenhao.Zhang@UTSouthwestern.edu

Xue-Xin Wei⁴
weixx@utexas.edu

Ying Nian Wu¹
ywu@stat.ucla.edu

¹Department of Statistics and Data Science, UCLA ²Google Deepmind

³Lyda Hill Department of Bioinformatics and O'Donnell Brain Institute, UT Southwestern Medical Center

⁴Departments of Neuroscience and Psychology, UT Austin

Abstract

This paper investigates the conformal isometry hypothesis as a potential explanation for the emergence of hexagonal periodic patterns in the response maps of grid cells. The hypothesis posits that the activities of the population of grid cells form a high-dimensional vector in the neural space, representing the agent's self-position in 2D physical space. As the agent moves in the 2D physical space, the vector rotates in a 2D manifold in the neural space, driven by a recurrent neural network. The conformal isometry hypothesis proposes that this 2D manifold in the neural space is a conformally isometric embedding of the 2D physical space, in the sense that local displacements of the vector in neural space are proportional to local displacements of the agent in the physical space. Thus the 2D manifold forms an internal map of the 2D physical space, equipped with an internal metric. In this paper, we conduct numerical experiments to show that this hypothesis underlies the hexagon periodic patterns of grid cells. We also conduct theoretical analysis to further support this hypothesis. In addition, we propose a conformal modulation of the input velocity of the agent so that the recurrent neural network of grid cells satisfies the conformal isometry hypothesis automatically. To summarize, our work provides numerical and theoretical evidences for the conformal isometry hypothesis for grid cells and may serve as a foundation for further development of normative models of grid cells and beyond.

1 Introduction

The mammalian hippocampus formation encodes a “cognitive map” (Tolman, 1948; O'Keefe and Nadel, 1979) of the animal's surrounding environment. In the 1970s, it was found that the rodent hippocampus contained place cells (O'Keefe and Dostrovsky, 1971), which typically fired at specific locations in the environment. Several decades later, another prominent type of neurons called grid cells (Hafting et al., 2005; Fyhn et al., 2008; Yartsev et al., 2011; Killian et al., 2012; Jacobs et al., 2013; Doeller et al., 2010) were discovered in the medial entorhinal cortex. Each grid cell fires at multiple locations that form a hexagonal periodic grid over the field (Fyhn et al., 2004; Hafting et al., 2005; Fuhs and Touretzky, 2006; Burak and Fiete, 2009; Sreenivasan and Fiete, 2011; Blair et al., 2007; Couey et al., 2013; de Almeida et al., 2009; Pastoll et al., 2013; Agmon and Burak, 2020). Grid cells interact with place cells and are believed to be involved in path integration (Hafting et al., 2005; Fiete et al., 2008; McNaughton et al., 2006; Gil et al., 2018; Ridler et al., 2019; Horner et al., 2016;

Ginosar et al., 2023; Boccara et al., 2019), which calculates the agent’s self-position by accumulating its self-motion. Thus, grid cells are often considered to form an internal Global Positioning System (GPS) in the brain (Moser and Moser, 2016). While grid cells were mostly studied in the spatial domain, it was proposed that grid-like response may also exist in non-spatial and more abstract cognitive spaces (Constantinescu et al., 2016; Bellmund et al., 2018).

Various computational models have been proposed to explain the striking firing properties of grid cells. Traditional approach designed hand-crafted continuous attractor neural networks (CANN) (Amit, 1992; Burak and Fiete, 2009; Couey et al., 2013; Pastoll et al., 2013; Agmon and Burak, 2020) and studied them by numerical simulation. More recently two pioneering papers (Cueva and Wei, 2018; Banino et al., 2018) learned recurrent neural networks (RNNs) on path integration tasks and demonstrated that grid patterns emerge in the learned networks. These results have been further developed in (Gao et al., 2019; Sorscher et al., 2019; Cueva et al., 2020; Gao et al., 2021; Whittington et al., 2021; Dorrell et al., 2022; Xu et al., 2022; Sorscher et al., 2023). In addition to RNN models, principal component analysis (PCA)-based basis expansion models (Dordek et al., 2016; Sorscher et al., 2023; Stachenfeld et al., 2017) with non-negativity constraints have been proposed to model the interaction between grid cells and place cells.

While prior work has shed much light on the grid cells, the mathematical principle that underlie the emergence of hexagon grid patterns are still not well understood (Cueva and Wei, 2018; Sorscher et al., 2023; Gao et al., 2021; Nayebe et al., 2021; Schaeffer et al., 2022). The goal of this paper is to investigate a conformal isometry hypothesis as a possible mathematical principle that explains the emergence of hexagon periodic patterns of the response maps of grid cells.

The conformal isometry hypothesis was formalized by Xu et al. (2022) and was explored earlier in Gao et al. (2021, 2019). It was adapted in the recent work of Schaeffer et al. (2023), and was investigated by Schoyen et al. (2024) for a class of Fourier-based models. Our work follows the development of Xu et al. (2022); Gao et al. (2021). While in Xu et al. (2022); Gao et al. (2021), conformal isometry is studied within a model class that consists of both place cells and grid cells, in this paper, we take a step back and focus our attention on the conformal isometry hypothesis within a minimalistic setting that consists of a single module of grid cells equipped with an explicit metric. This reductionism approach allows us to put the conformal isometry hypothesis to the forefront, and gain a sharpened and deeper understanding of the hypothesis.

The conformal isometry hypothesis posits that the activities of the population of grid cells form a high-dimensional vector in the neural space, representing the agent’s self-position in 2D physical space. As the agent moves in the 2D physical space, the vector rotates in a 2D manifold in the neural space, driven by a recurrent neural network. The conformal isometry hypothesis proposes that this 2D manifold in the neural space is a conformally isometric embedding of the 2D physical space, in the sense that the local displacement of the vector in the neural space is proportional to the corresponding local displacement of the agent in the physical space. As a consequence, the 2D Euclidean space is embedded conformally as a 2D manifold in the neural space, and this 2D manifold forms an internal map of the 2D physical environment, equipped with an internal metric, thus mathematically realizing the notion that grid cells form an internal GPS (Moser and Moser, 2016).

In this paper, we conduct numerical experiments in the aforementioned minimalistic setting to show that the conformal isometry hypothesis underlies the hexagon periodic patterns of the response maps of grid cells. We also conduct theoretical analysis to further support this hypothesis.

While our minimalistic setting is concerned with a single module of grid cells, we also study composing multiple modules of grid cells and decode them to the adjacency kernels that model the place cells. For that purpose, we further propose a conformal modulation mechanism that modulates the input velocity of the agent so that the recurrent neural network of grid cells satisfies the conformal isometry hypothesis automatically without any further constraint. Numerical experiments show that the learned model is capable of accurate path integration.

Contributions. To summarize, our paper investigates the conformal isometry hypothesis as a possible mathematical principle that underlies grid cell system. Our contributions are as follows. (1) We conduct a systematic numerical study of the conformal isometry hypothesis under the minimalistic setting of a single module of grid cells. (2) We conduct theoretical analysis that supports the conformal isometry hypothesis. (3) We propose a conformal modulation mechanism for the recurrent neural

network of grid cells that leads to conformal isometry. It is our hope that our work may serve as a foundation for further development of normative models of grid cells and beyond.

2 Background

2.1 Representing self-position

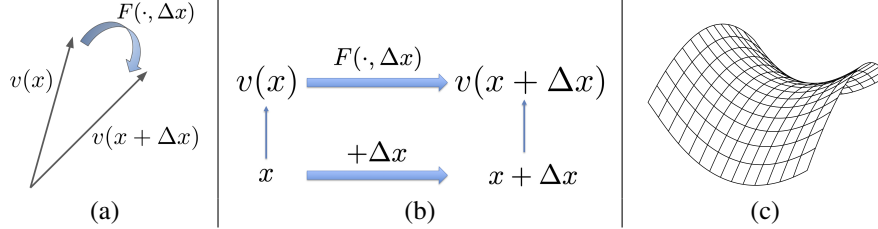


Figure 1: (a) The self-position $\mathbf{x} = (x_1, x_2)$ in 2D Euclidean space is represented by a vector $\mathbf{v}(\mathbf{x})$ in the d -dimensional neural space. When the agent moves by $\Delta \mathbf{x}$, the vector is transformed to $\mathbf{v}(\mathbf{x} + \Delta \mathbf{x}) = F(\mathbf{v}(\mathbf{x}), \Delta \mathbf{x})$. (b) $F(\cdot, \Delta \mathbf{x})$ is a representation of the self-motion $\Delta \mathbf{x}$. (c) $M = (\mathbf{v}(\mathbf{x}), \mathbf{x} \in D)$ is a 2D manifold in the neural space, and is an embedding of the 2D Euclidean domain D (shape in the figure is merely illustrative).

Suppose the agent is at the self-position $\mathbf{x} = (x_1, x_2) \in \mathbb{R}^2$ within a 2D Euclidean domain D . The activities of the population of d grid cells form a d -dimensional vector $\mathbf{v}(\mathbf{x}) = (v_i(\mathbf{x}), i = 1, \dots, d)$, where $v_i(\mathbf{x})$ is the activity of the i -th grid cell at position \mathbf{x} . We call the d -dimensional vector space of \mathbf{v} the neural space, and we embed \mathbf{x} in the 2D physical space as a vector $\mathbf{v}(\mathbf{x})$ in the d -dimensional neural space. For each grid cell i , $v_i(\mathbf{x})$, as a function of \mathbf{x} , represents the response map of grid cell i . The response maps of grid cells exhibit periodic hexagonal grid patterns.

2.2 Representing self-motion

At self-position $\mathbf{x} = (x_1, x_2)$, assume the agent makes a movement $\Delta \mathbf{x} = (\Delta x_1, \Delta x_2)$ and moves to $\mathbf{x} + \Delta \mathbf{x}$. Correspondingly, the vector $\mathbf{v}(\mathbf{x})$ is transformed to $\mathbf{v}(\mathbf{x} + \Delta \mathbf{x})$. The general form of the transformation can be formulated as:

$$\mathbf{v}(\mathbf{x} + \Delta \mathbf{x}) = F(\mathbf{v}(\mathbf{x}), \Delta \mathbf{x}), \quad (1)$$

where F can be parametrized by a recurrent neural network (RNN). See Figure 1(a). The input velocity $\Delta \mathbf{x}$ can also be represented as $(\Delta r, \theta)$ in polar coordinates, where $\Delta r = \|\Delta \mathbf{x}\|$ is the displacement along the heading direction $\theta \in [0, 2\pi]$, so that $\Delta \mathbf{x} = (\Delta x_1 = \Delta r \cos \theta, \Delta x_2 = \Delta r \sin \theta)$. $F(\cdot, \Delta \mathbf{x})$ is a representation of the self-motion $\Delta \mathbf{x}$. See Figure 1(b). We can also write $F(\mathbf{v}(\mathbf{x}), \Delta \mathbf{x}) = F(\mathbf{v}(\mathbf{x}), \Delta r, \theta)$ with slight overloading of notation F . The transformation model is necessary for path integration and path planning.

2.3 Conformal isometry

For each $\mathbf{x} \in D$, where D is the 2D Euclidean domain, such as a $1\text{m} \times 1\text{m}$ square, we embed \mathbf{x} as a vector $\mathbf{v}(\mathbf{x})$ in the d -dimensional neural space. Collectively, $M = (\mathbf{v}(\mathbf{x}), \forall \mathbf{x} \in D)$ is a 2D manifold in the neural space, and M is an embedding of D . See Figure 1(b) (the shape of M in the figure is merely illustrative). As the agent moves in D , $\mathbf{v}(\mathbf{x})$ moves in M .

The conformal isometry hypothesis (Xu et al., 2022; Gao et al., 2021) proposes that M is a conformal embedding of D . Specifically, at any $\mathbf{x} \in D$, for a local $\Delta \mathbf{x}$, we have

$$\|\mathbf{v}(\mathbf{x} + \Delta \mathbf{x}) - \mathbf{v}(\mathbf{x})\| = s \|\Delta \mathbf{x}\|, \quad (2)$$

where s is a constant scaling factor that is independent of \mathbf{x} and $\Delta \mathbf{x}$. Thus as the agent moves in D by $\|\Delta \mathbf{x}\|$, the vector $\mathbf{v}(\mathbf{x})$ moves in M by $s \|\Delta \mathbf{x}\|$. s serves as a metric; larger s corresponds to a finer metric. For a constant s , the intrinsic geometry of M remains Euclidean or flat, i.e., up to a global scaling factor s , M is a folding or bending of the flat D without distorting stretching or squeezing.

An internal map with a metric. Combining of the above 3 subsections, the population of grid cells form an internal map equipped with an internal metric, with $\mathbf{v}(\mathbf{x})$ representing \mathbf{x} , $F(\cdot, \Delta\mathbf{x})$ representing $\Delta\mathbf{x}$, and with the scale s determining the metric or resolution of the map.

3 A minimalistic setting

3.1 Assumptions

In this section, we seek to study the grid cell system with a minimal number of assumptions. Specifically, we make the following 4 assumptions:

Assumption 1. Conformal isometry: $\|\mathbf{v}(\mathbf{x} + \Delta\mathbf{x}) - \mathbf{v}(\mathbf{x})\| = s\|\Delta\mathbf{x}\|$. In the minimalistic setting, we specify s explicitly, in order to understand how s affects the learned hexagon patterns, and conversely what the hexagon patterns reveal about the underlying s . This will enable us to gain a deeper geometric understanding of the grid cell patterns. We shall discuss learning s in Section 5.

Assumption 2. Transformation: $\mathbf{v}(\mathbf{x} + \Delta\mathbf{x}) = F(\mathbf{v}(\mathbf{x}), \Delta\mathbf{x})$, where F is a recurrent neural network. We want to be agnostic about F , and our numerical experiments show that hexagon grid patterns emerge regardless of the form of F . In our experiments, we consider the following simple forms.

(1) Linear model: $\mathbf{v}(\mathbf{x} + \Delta\mathbf{x}) = \mathbf{v}(\mathbf{x}) + \mathbf{B}(\theta)\mathbf{v}(\mathbf{x})\Delta r$, where $\Delta r = \|\Delta\mathbf{x}\|$ is the displacement, and θ is the heading direction of $\Delta\mathbf{x}$. $\mathbf{B}(\theta)$ is a $d \times d$ square matrix.

(2) Nonlinear model 1: $\mathbf{v}(\mathbf{x} + \Delta\mathbf{x}) = R(\mathbf{A}\mathbf{v}(\mathbf{x}) + \mathbf{B}(\theta)\mathbf{v}(\mathbf{x})\Delta r + \mathbf{b})$, where R is elementwise nonlinearity such as ReLU or Tanh, \mathbf{A} and $\mathbf{B}(\theta)$ are $d \times d$ square matrices, and \mathbf{b} is the $d \times 1$ bias vector.

(3) Nonlinear model 2: $\mathbf{v}(\mathbf{x} + \Delta\mathbf{x}) = R(\mathbf{A}\mathbf{v}(\mathbf{x}) + \mathbf{B}(\theta)\Delta r + \mathbf{b})$, where $\mathbf{B}(\theta)$ is a $d \times 1$ vector, \mathbf{b} is the bias vector, and R is nonlinearity.

In the above models, $\mathbf{B}(\theta)\Delta r$ can also be replaced by $\mathbf{B}_1\Delta x_1 + \mathbf{B}_2\Delta x_2$ if we use a cartesian coordinate system $\mathbf{x} = (x_1, x_2)$, where $(\mathbf{B}_1, \mathbf{B}_2)$ shares the same dimensionality as $\mathbf{B}(\theta)$. We can also include quadratic or polynomial terms in Δr or $(\Delta x_1, \Delta x_2)$ with matrix or vector coefficients.

Assumption 3. Normalization: $\|\mathbf{v}(\mathbf{x})\| = 1$ for each $\mathbf{x} \in D$. $\|\mathbf{v}(\mathbf{x})\|^2 = \sum_i v_i(\mathbf{x})^2$ can be interpreted as the total energy of the population of neurons in \mathbf{v} at position \mathbf{x} . This normalization assumption makes the conformal isometry assumption well defined. Otherwise, we can multiply the vector $\mathbf{v}(\mathbf{x})$ by an arbitrary constant c , so that the scaling factor s is changed to cs . Such undesirable arbitrariness is eliminated by the normalization assumption. Under this assumption, the embedding manifold M resides in a high-dimensional unit sphere, so that the conformal isometry assumption can also be expressed in terms of angle:

$$\langle \mathbf{v}(\mathbf{x}), \mathbf{v}(\mathbf{x} + \Delta\mathbf{x}) \rangle = \cos(s\|\Delta\mathbf{x}\|), \quad (3)$$

i.e., as the agent moves by $\Delta\mathbf{x}$, the vector $\mathbf{v}(\mathbf{x})$ rotates by an angle $s\|\Delta\mathbf{x}\|$.

Assumption 4. Non-negativity: $v_i(\mathbf{x}) \geq 0$ for each i and \mathbf{x} . This is the assumption studied by Dordek et al. (2016); Sorscher et al. (2023); Stachenfeld et al. (2017). It is obviously true for biological neurons. However, our ablation studies show that it is not necessary for the emergence of hexagon grid patterns. On the other hand, this assumption does enable more stable learning of clean patterns, because it greatly constrains the solution space.

The above assumptions form a minimalistic setting for studying grid cells, where place cells are not involved. This enables us to study the grid cells in isolation with an explicit metric s .

3.2 Learning method

Let D be a $1\text{m} \times 1\text{m}$ Euclidean continuous square domain. We overlay a 40×40 regular grid on D . We learn $\mathbf{v}(\mathbf{x})$ on the 40×40 grid points, but we treat \mathbf{x} as continuous, so that for \mathbf{x} off the grid points, we let $\mathbf{v}(\mathbf{x})$ be the bi-linear interpolation of the $\mathbf{v}(\mathbf{x})$ on the 4 nearest grid points. We also learn the parameters in the transformation model F , where we discretize the direction θ .

The loss function consists of the following two terms:

$$L_1 = \mathbb{E}_{\mathbf{x}, \Delta\mathbf{x}} [(\|\mathbf{v}(\mathbf{x} + \Delta\mathbf{x}) - \mathbf{v}(\mathbf{x})\| - s\|\Delta\mathbf{x}\|)^2], \quad (4)$$

$$L_2 = \mathbb{E}_{\mathbf{x}, \Delta\mathbf{x}} [\|\mathbf{v}(\mathbf{x} + \Delta\mathbf{x}) - F(\mathbf{v}(\mathbf{x}), \Delta\mathbf{x})\|^2], \quad (5)$$

where L_1 is to satisfy the Assumption 1 on conformal isometry, and L_2 is to satisfy the Assumption 2 on transformation. We can also let L_1 be

$$L_1 = \mathbb{E}_{\mathbf{x}, \Delta \mathbf{x}} [(\langle \mathbf{v}(\mathbf{x} + \Delta \mathbf{x}), \mathbf{v}(\mathbf{x}) \rangle - \cos(s \|\Delta \mathbf{x}\|))^2]. \quad (6)$$

Numerical results from the two versions of L_1 are very similar in our experiments. Since L_2 is a one-step transformation loss, there is no need for back-propagation through time.

We minimize $L = L_1 + \lambda L_2$ over the set of $\mathbf{v}(\mathbf{x})$ on the 40×40 grid points as well as the parameters in F , such as $\mathbf{B}(\theta)$ for the discrete set of directions θ in the linear model. $\lambda > 0$ is a hyper-parameter that balances L_1 and L_2 . We use stochastic gradient descent to minimize L , where in each iteration, the expectations in L are replaced by the averages over Monte Carlo samples of $(\mathbf{x}, \Delta \mathbf{x})$.

After each iteration, we set negative values in the elements of each $\mathbf{v}(\mathbf{x})$ to zero to enforce the Assumption 4 on non-negativity, and then we normalize $\mathbf{v}(\mathbf{x})$ for each \mathbf{x} to have norm 1 to enforce the Assumption 3 on normalization.

3.3 Numerical experiments

We conducted numerical experiments for the minimalistic setting. To demonstrate its generality, we applied our method to several model parameterizations with different activation functions. Additionally, we varied the scaling factor s and the number of neurons. For $\Delta \mathbf{x}$ in L_1 , we constrained $\Delta \mathbf{x}$ to be local so that $s \|\Delta \mathbf{x}\| \leq c$ where $c = 1.25$ in our experiments. For L_2 , $\|\Delta \mathbf{x}\|$ was restricted to be smaller than 3 grids.

The dimensions of $\mathbf{v}(\mathbf{x})$, representing the total number of grid cells, were nominally set to 24 for both the linear model and nonlinear model 1, and 1000 for nonlinear model 2. Notably, similar results can be obtained with different numbers of cells, e.g., 500, for both the linear model and nonlinear model 1. All the parameters are updated by Adam (Kingma and Ba, 2014) optimizer.

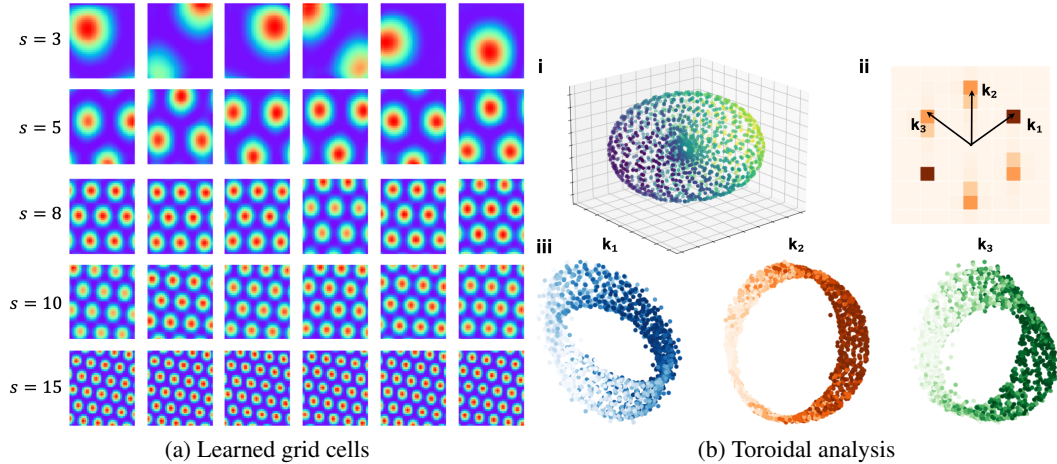


Figure 2: Hexagonal patterns learned in linear models. (a) Learned patterns of linear model with different scales. (b) Toroidal structure spectral analysis of the activities of grid cells.

Hexagonal patterns. We first trained the linear model with manually assigned scaling factor s by minimizing $L = L_1 + \lambda L_2$. Figure 2(a) shows the learned firing patterns of $\mathbf{v}(\mathbf{x})$ over the 40×40 lattice of \mathbf{x} for linear models with the change of scaling factors s , which controlled the scale or metric of the lattice. In Figure 2(a), each image represents the response map for a grid cell, with each row displaying 6 randomly sampled response maps. The emergence of hexagonal patterns in these activity patterns is evident. Consistency in scale and orientation is observed within each scale, though variations in phases or spatial shifts are apparent.

Additionally, we trained nonlinear models with different activation functions. Figures 3(a-d) show that hexagonal patterns also emerge with nonlinear transformations, indicating that the grid-like patterns are stable and easy to learn regardless of the form of transformation, grid scales, and the total number of neurons.

Table 1: Gridness scores and validity rates of grid cells in learned models. The last two rows represent the results of our models.

MODEL	GRIDNESS	VALID RATE
BANINO ET AL. (2018)	0.18	25.2%
SORSCHER ET AL. (2023)	0.48	56.1%
GAO ET AL. (2021)	0.90	73.1%
OUR LINEAR	1.70	100.0%
OUR NONLINEAR	1.17	100.0%

Table 2: Scaling factor s and estimated scale for learned patterns in single-module linear models.

SCALING FACTOR	ESTIMATED SCALE
$s = 5$	0.82
$s = 10$	0.41
$s = 15$	0.27

To evaluate how closely the learned patterns align with regular hexagonal grids, we recruited the most commonly used metric for quantifying grid cells, the gridness score, adopted by the neuroscience literature (Langston et al., 2010; Sargolini et al., 2006). The gridness scores and the successful rate were reported in Table 1. Compared to other existing learning-based approaches, our models exhibit notably high gridness scores (\uparrow) and a high percentage of valid grid cells (\uparrow).

We also investigated the relationship between the manually assigned scaling factor s and the estimated scale of the learned patterns following (Langston et al., 2010; Sargolini et al., 2006). As shown in Table 2, the estimated scale of the learned patterns is proportional to $1/s$ almost exactly.

Topological analysis. As discussed in Section 4, the joint activities of grid cells should reside on a torus-like manifold, and the positions on the torus correspond to the physical locations of a moving agent. To evaluate whether our empirically learned representations align with the topological properties of theoretical models, we employed a nonlinear dimension reduction method (spectral embedding Saul et al. (2006)) to show that grid cell states fell on a toroidal manifold as depicted in Figure 2b(i). To further investigate periodicity and orientation within the same module, we conducted numerical simulations of pattern forming dynamics. In Figure 2b(ii), we applied 2D Fourier transforms of the learned maps, revealing that the Fourier power is hexagonally distributed along 3 principal directions k_1 , k_2 , and k_3 . Following Schøyen et al. (2022); Schaeffer et al. (2023), projecting the toroidal manifold onto the 3 vectors, we can observe 3 rings in Figure 2b(iii). This indicates the manifold has a 2D twisted torus topology.

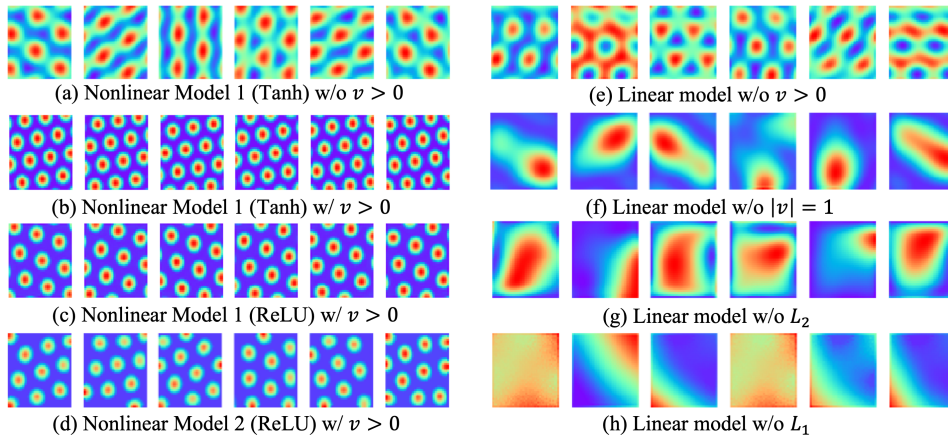


Figure 3: *Left*(a-d): Learned patterns for nonlinear models with different rectified functions. *Right*(e-h): Ablation for linear model.

Ablation study. We show ablation results to investigate the empirical significance of each assumption for the emergence of hexagon grid patterns. First, we highlight the essential role of conformal isometry; in its absence, as shown in Figure 3(h), the response maps display non-hexagon patterns. Next, as shown in Figure 3(a) and (e), we also ablate the non-negative assumption. Without $v(\mathbf{x}) \geq 0$, the hexagonal pattern still emerge. For the transformation and normalization assumptions, Figure 3(f) and (g) indicate that they are necessary.

4 Theoretical understanding

4.1 Torus topology

The transformations $(F(\cdot, \Delta\mathbf{x}), \forall \Delta\mathbf{x})$ form a group acting on the manifold $M = (\mathbf{v}(\mathbf{x}), \forall \mathbf{x})$. The group $(F(\cdot, \Delta\mathbf{x}), \forall \Delta\mathbf{x})$ is a representation of the 2D additive Euclidean group $(\mathbb{R}^2, +)$, i.e., $F(\mathbf{v}(\mathbf{x}), \Delta\mathbf{x}_1 + \Delta\mathbf{x}_2) = F(F(\mathbf{v}(\mathbf{x}), \Delta\mathbf{x}_1), \Delta\mathbf{x}_2) = F(F(\mathbf{v}(\mathbf{x}), \Delta\mathbf{x}_2), \Delta\mathbf{x}_1)$, $\forall \mathbf{x}, \Delta\mathbf{x}_1, \Delta\mathbf{x}_2$, and $F(\mathbf{v}(\mathbf{x}), 0) = \mathbf{v}(\mathbf{x})$, $\forall \mathbf{x}$ (Gao et al., 2021). See Figure 1(a) for an illustration. Since $(\mathbb{R}^2, +)$ is an abelian Lie group, $(F(\cdot, \Delta\mathbf{x}), \forall \Delta\mathbf{x})$ is also an abelian Lie group. Because of Assumption 3 on normalization, $\|\mathbf{v}(\mathbf{x})\| = 1$. Thus the manifold $(\mathbf{v}(\mathbf{x}), \forall \mathbf{x})$ is compact, and $(F(\cdot, \Delta\mathbf{x}), \forall \Delta\mathbf{x})$ is a compact group. It is also connected because the 2D domain is connected. According to a classical theorem in Lie group theory (Dwyer and Wilkerson, 1998), a compact and connected abelian Lie group has a topology of a torus. The torus topology is supported by neuroscience data (Gardner et al., 2021) as well as our numerical experiments.

4.2 Periodic function

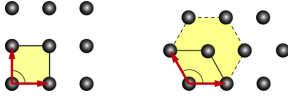


Figure 4: Square lattice and hexagon lattice.

Since \mathbf{x} and $\Delta\mathbf{x}$ are 2D, the torus formed by $(F(\cdot, \Delta\mathbf{x}), \forall \Delta\mathbf{x})$ is 2D, then its topology is $\mathbb{S}_1 \times \mathbb{S}_1$, where each \mathbb{S}_1 is a circle. Thus we can find two 2D vectors $\Delta\mathbf{x}_1$ and $\Delta\mathbf{x}_2$, so that $F(\cdot, \Delta\mathbf{x}_1) = F(\cdot, \Delta\mathbf{x}_2) = F(\cdot, 0)$. As a result, $\mathbf{v}(\mathbf{x})$ is a 2D periodic function so that $\mathbf{v}(\mathbf{x} + k_1\Delta\mathbf{x}_1 + k_2\Delta\mathbf{x}_2) = \mathbf{v}(\mathbf{x})$ for arbitrary integers k_1 and k_2 . We assume $\Delta\mathbf{x}_1$ and $\Delta\mathbf{x}_2$ are the shortest vectors that characterize the above 2D periodicity. According to the theory of 2D Bravais lattice (Ashcroft et al., 1976) (see Appendix A.4 for details), any 2D periodic lattice can be defined by two primitive vectors $(\Delta\mathbf{x}_1, \Delta\mathbf{x}_2)$.

If the scaling factor s is constant, then as the position \mathbf{x} of the agent moves from 0 to $\Delta\mathbf{x}_1$ in the 2D space, $\mathbf{v}(\mathbf{x})$ traces a perfect circle of circumference $s\|\Delta\mathbf{x}_1\|$ in the neural space due to conformal isometry, i.e., the geometry of the trajectory of $\mathbf{v}(\mathbf{x})$ is a perfect circle up to bending or folding but without distortion by stretching. The same with movement from 0 to $\Delta\mathbf{x}_2$. Since we normalize $\|\mathbf{v}(\mathbf{x})\| = 1$, the two circles have the same radius 1 and thus they also have the same circumferences 2π , hence we have $\|\Delta\mathbf{x}_1\| = \|\Delta\mathbf{x}_2\| = 2\pi/s$. According to Bravais lattice theory (Ashcroft et al., 1976), the periodic lattice with two equal-length primitive vectors can only be square or hexagon, as illustrated by Figure 4.

4.3 Fourier analysis

The Fourier transform of a 2D period function $f(\mathbf{x})$ can be written as a linear superposition of Fourier components $f(\mathbf{x}) = \sum_k \hat{f}(\omega_k) e^{i\langle \omega_k, \mathbf{x} \rangle}$, where $\omega_k = k_1\mathbf{a}_1 + k_2\mathbf{a}_2$, $k = (k_1, k_2)$ are two integers, and $(\mathbf{a}_1, \mathbf{a}_2)$ are primitive vectors in the reciprocal space. For square or hexagon lattice with $\|\Delta\mathbf{x}_1\| = \|\Delta\mathbf{x}_2\| = \rho = 2\pi/s$, we have $\|\mathbf{a}_1\| = \|\mathbf{a}_2\| = 2\pi/\rho = s$, and the lattice in the reciprocal space remains to be square or hexagon respectively.

Discrete set of rings in frequency domain. For either square or hexagon lattice, the set of $(\omega_k, \forall k = (k_1, k_2))$ lie on a discrete set of rings, i.e., $\|\omega_k\|$ take a discrete set of values. On each ring, for the square case, ω_k form two orthogonal axes, i.e., superposition of two plane waves in perpendicular directions. For the hexagon case, ω_k form three equal spacing axes of $2\pi/3$ apart, i.e., superposition of three plane waves in three equal-spacing directions.

Square vs hexagon. To compare square and hexagon periodicity, let us focus on a single ring of fixed norm. On this ring, the square case has $\|\mathbf{a}_1\| = \|\mathbf{a}_2\|$ and $\mathbf{a}_1 \perp \mathbf{a}_2$, whereas the hexagon case has \mathbf{a}_1 and \mathbf{a}_2 of the same norm s but $2\pi/3$ apart, and it also has $\mathbf{a}_3 = -(\mathbf{a}_1 + \mathbf{a}_2)$ which has the same norm. $(\mathbf{a}_1, \mathbf{a}_2, \mathbf{a}_3)$ together forms 3 equal spacing basis vectors in 2D. It is a iconic example of an over-complete tight frame, which generalizes orthogonal basis in the square case.

Consider the following prototype model $\mathbf{v}(\mathbf{x}) = c\mathbf{U}e(\mathbf{x})$, where $e(\mathbf{x}) = (e^{i\langle \mathbf{a}_k, \mathbf{x} \rangle}, k = 1, \dots, d)$ is a d -dimensional vector with $d = 2$ for square and $d = 3$ for hexagon, \mathbf{U} is a $d \times d$ unitary matrix, and c is an arbitrary scalar. Such a prototype model was studied in Gao et al. (2021), which shows $\mathbf{v}(\mathbf{x})$ satisfies the linear transformation model.

We obtain an interesting new result which shows that for the hexagon periodic $v(\mathbf{x})$, $\langle v(\mathbf{x} + \Delta\mathbf{x}), v(\mathbf{x}) \rangle$ is isotropic up to $\|\Delta\mathbf{x}\|^4$, whereas for square periodic $v(\mathbf{x})$, $\langle v(\mathbf{x} + \Delta\mathbf{x}), v(\mathbf{x}) \rangle$ is isotropic only up to $\|\Delta\mathbf{x}\|^2$. See Appendix A.3 for a detailed calculation.

For general high-dimensional $v(\mathbf{x})$, it can be obtained by concatenating the above $v(\mathbf{x})$ for rings of different frequencies (each obtained by its own cU), followed by rotation of the concatenated vector by a unitary matrix operating on the concatenated vector. Such a general $v(\mathbf{x})$ is again isotropic up to $\|\Delta\mathbf{x}\|^4$ for hexagon periodic $v(\mathbf{x})$. Because conformal isometry is isotropic, hexagon periodic $v(\mathbf{x})$ is preferred.

4.4 Permutation group and relation to attractor network

The learned response maps of the grid cells in the same module are shifted versions of each other, i.e., there is a discrete set of displacements $\{\Delta\mathbf{x}\}$, such as for each $\Delta\mathbf{x}$ in this set, we have $v_i(\mathbf{x} + \Delta\mathbf{x}) = v_j(\mathbf{x})$, where $j = \sigma(i, \Delta\mathbf{x})$, and σ is a mapping from i to j that depends on $\Delta\mathbf{x}$. In other words, $\Delta\mathbf{x}$ causes a permutation of the indices of the elements in $v(\mathbf{x})$, and $F(\cdot, \Delta\mathbf{x}) \cong \sigma(\cdot, \Delta\mathbf{x})$, that is, the transformation group for the discrete set of $\Delta\mathbf{x}$ is equivalent to a subgroup of the permutation group. This is consistent with hand-designed CANN (Amit, 1992; Burak and Fiete, 2009; Couey et al., 2013; Pastoll et al., 2013; Agmon and Burak, 2020). A CANN places grid cells on a 2D “neuron sheet” with periodic boundary condition, i.e., a 2D torus, and lets the movement of the “bump” formed by the activities of grid cells mirror the movement of the agent in a conformal way, and the movement of the “bump” amounts to cyclic permutation of the neurons. Our model does not assume such an *a priori* 2D torus neuron sheet, and is much simpler and more generic.

5 Composing multiple modules with learned metrics

5.1 Multiple modules

The minimalistic setting studied in the previous sections is about a single module of grid cells. The grid cells form multiple modules or blocks (Barry et al., 2007; Stensola et al., 2012), and the response maps of grid cells within each module share the same scale and orientation. Each module forms a map of the 2D domain with a metric s . Different modules form maps of the 2D domain with different metrics as well as orientations.

Paving the frequency domain. In the Fourier analysis of the previous section, each module of scale s consists of Fourier components whose frequencies form a hexagon grid, with the lowest frequencies having norm s . We thus need multiple modules of different scales and orientations to pave the whole frequency domain. Hexagon grid is superior than square grid because the former leads to denser packing of frequency components.

Linear decoding. Let $v(\mathbf{x}) = (v_k(\mathbf{x}), k = 1, \dots, K)$ be the vector that consists of K sub-vectors, with each sub-vector $v_k(\mathbf{x})$ being a module studied in the minimalistic setting. If the multiple modules pave the frequency domain, then $v(\mathbf{x})$ can be linearly decoded into any nonlinear function of \mathbf{x} . Specifically, let $f(\mathbf{x})$ be any nonlinear function of \mathbf{x} , then we can linearly expand $f(\mathbf{x})$ in terms of $v(\mathbf{x})$: $f(\mathbf{x}) = \langle \mathbf{w}, v(\mathbf{x}) \rangle = \sum_k \langle \mathbf{w}_k, v_k(\mathbf{x}) \rangle$, where $\mathbf{w} = (\mathbf{w}_k, k = 1, \dots, K)$ is the vector of coefficients, with \mathbf{w}_k being the sub-vector for $v_k(\mathbf{x})$.

Multi-module: emergent or inductive bias? We argue that multiple modules can be treated as multi-scale design choice or inductive bias, similar to multi-layer, multi-channel, convolutional kernel design of convolutional neural network.

Place cells. A particular set of nonlinear functions are the adjacencies between position \mathbf{x} and other positions \mathbf{x}' . Specifically, define the adjacency kernel $A(\mathbf{x}, \mathbf{x}') = \exp(-\|\mathbf{x} - \mathbf{x}'\|^2/2\sigma^2)$ for a certain scale parameter σ . $A(\mathbf{x}, \mathbf{x}')$ is a model of the response map (as a function of \mathbf{x}) of a place cell for the place \mathbf{x}' . We can then use $v(\mathbf{x})$ to decode A via $A(\mathbf{x}, \mathbf{x}') = \langle \mathbf{w}(\mathbf{x}'), v(\mathbf{x}) \rangle$, where $\mathbf{w}(\mathbf{x}')$ is the decoding vector associated with place cell \mathbf{x}' . Given $A(\mathbf{x}, \mathbf{x}')$, we can learn $v(\mathbf{x})$.

5.2 Conformal modulation of input velocity

For notation simplicity, we use $v(\mathbf{x})$ to denote a single module in this subsection. Consider the general recurrent transformation $v(\mathbf{x} + \Delta\mathbf{x}) = F(v(\mathbf{x}), \Delta\mathbf{x}) = F(v(\mathbf{x}), \Delta r, \theta)$, where $\Delta\mathbf{x} =$

($\Delta x_1 = \Delta r \cos \theta$, $\Delta x_2 = \Delta r \sin \theta$), θ is the heading direction, and Δr is the displacement, the directional derivative of F at (\mathbf{v}, θ) is defined as

$$f(\mathbf{v}, \theta) = \frac{\partial}{\partial a} F(\mathbf{v}, a, \theta) |_{a=0}. \quad (7)$$

With the above definition, the first order Taylor expansion of the recurrent transformation at $\Delta r = 0$ gives us

$$\mathbf{v}(\mathbf{x} + \Delta \mathbf{x}) = \mathbf{v}(\mathbf{x}) + f(\mathbf{v}(\mathbf{x}), \theta) \Delta r + o(\Delta r). \quad (8)$$

The conformal modulation of Δr is defined as

$$\overline{\Delta r} = \frac{s}{\|f(\mathbf{v}(\mathbf{x}), \theta)\|} \Delta r, \quad (9)$$

where $\|\cdot\|$ is the ℓ_2 norm, and s is a learnable parameter. With conformal modulation, the transformation is changed to

$$\mathbf{v}(\mathbf{x} + \Delta \mathbf{x}) = \overline{F}(\mathbf{v}(\mathbf{x}), \Delta r, \theta) = F(\mathbf{v}(\mathbf{x}), \overline{\Delta r}, \theta). \quad (10)$$

Then the first order Taylor expansion gives

$$\mathbf{v}(\mathbf{x} + \Delta \mathbf{x}) = \mathbf{v}(\mathbf{x}) + f(\mathbf{v}(\mathbf{x}), \theta) \overline{\Delta r} + o(\Delta r) = \mathbf{v}(\mathbf{x}) + s \overline{f}(\mathbf{v}(\mathbf{x}), \theta) \Delta r + o(\Delta r), \quad (11)$$

where $\overline{f}(\mathbf{v}, \theta) = f(\mathbf{v}, \theta) / \|f(\mathbf{v}, \theta)\|$ is a unit vector with $\|\overline{f}(\mathbf{v}, \theta)\| = 1$, which leads to $\|\mathbf{v}(\mathbf{x} + \Delta \mathbf{x}) - \mathbf{v}(\mathbf{x})\| = s \|\Delta \mathbf{x}\| + o(\|\Delta \mathbf{x}\|)$, i.e., conformal isometry. Thus $\overline{F}(\mathbf{v}(\mathbf{x}), \Delta r, \theta) = F(\mathbf{v}(\mathbf{x}), \Delta \mathbf{x})$ satisfies conformal isometry automatically.

5.3 Learning

We assume multiple modules, each has its own transformation with conformal modulation. The loss consists of two terms:

$$L_0 = \mathbb{E}_{\mathbf{x}, \mathbf{x}'} [(A(\mathbf{x}, \mathbf{x}') - \langle \mathbf{w}(\mathbf{x}'), \mathbf{v}(\mathbf{x}) \rangle)^2], \quad (12)$$

$$L_2 = \mathbb{E}_{\mathbf{x}, \Delta \mathbf{x}} [\|\mathbf{v}(\mathbf{x} + \Delta \mathbf{x}) - \overline{F}(\mathbf{v}(\mathbf{x}), \Delta \mathbf{x})\|^2], \quad (13)$$

where $\overline{F}(\cdot)$ is the transformation after conformal modulation, so that we do not need conformal isometry loss term L_1 . We assume $\mathbf{w}(\mathbf{x}') \geq 0$ because the connections from grid cells to place cells are excitatory (Zhang et al., 2013; Rowland et al., 2018). We do not enforce non-negativity of $\mathbf{v}(\mathbf{x})$. We continue to enforce $\|\mathbf{v}(\mathbf{x})\| = 1$.

In the numerical experiments, $A(\mathbf{x}, \mathbf{x}')$ is the given input, and we jointly learn the position embedding $\mathbf{v}(\mathbf{x})$, read-out weights $\mathbf{w}(\mathbf{x}')$, and the transformation model F by minimizing the total loss: $L = L_0 + \lambda_1 L_2$.

5.4 Numerical experiments

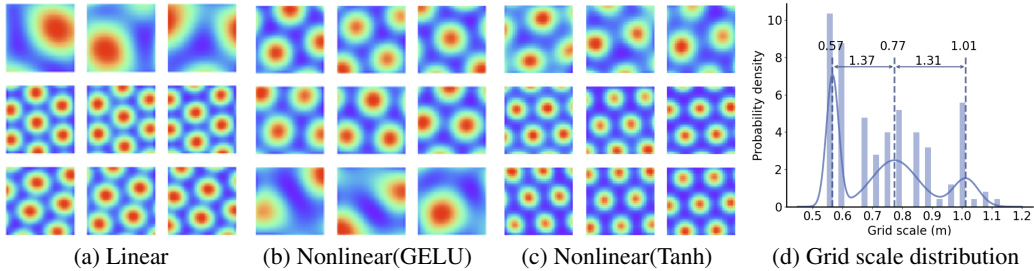


Figure 5: Results of linear and nonlinear models with GELU and Tanh activations and grid scale distribution.

We conducted numerical experiments to train multi-module models with linear and nonlinear transformations. The module size used was 24 cells for both models. We employed 15 modules for the linear

model and 8 modules for the nonlinear model. For the response maps of the place cells, we used a Gaussian adjacency kernel with $\sigma = 0.07$. Regarding the transformation, the one-step displacement Δr was set to be smaller than 3 grids. The scaling factor s was treated as learnable parameter for each module.

As shown in Figure 5(a-c), each row shows the units belonging to the same module and we randomly present 3 cells in each module. The empirical results illustrate that multi-scale grid hexagonal grid firing patterns emerge in the learned $v(\mathbf{x})$ across all models with conformal modulation.

Additionally, Figure 5(d) shows the histogram of grid scales of the learned grid cell neurons, which follows a multi-modal distribution. The distribution is best fitted by a mixture of 3 Gaussians with means 0.57, 0.77, and 1.01. The ratios between successive modes are 1.37 and 1.31. The scale relationships in our learned grid patterns across modules align with both theoretical predictions (Stemmler et al., 2015; Wei et al., 2015) and empirical observations from rodent grid cells (Stensola et al., 2012).

6 Limitations

The minimalistic setting enables us to study a module of grid cells in isolation. However, we have not studied the interactions between grid cell system, place cell system, vision system, cognitive map, and path planning.

The idealized minimalistic setting assumes a global constant scaling factor s . We have not studied the deformations of the response maps of grid cells in more realistic settings through the lens of deformed local metric, i.e., $s = s(\mathbf{x}, \theta)$ depends on either position \mathbf{x} or heading direction θ or both.

7 Related work

Relation to Sorscher et al. (2019). Our minimalistic setting does not make any assumption about place cells, while Sorscher et al. (2019) assumes center-surround difference of Gaussian kernels for place cells (an assumption challenged by Schaeffer et al. (2022, 2023)), and this kernel constrains the frequency components on a ring. As we explained in Section 4.3, the frequency components of our $v(\mathbf{x})$ lie on a discrete set of rings due to conformal isometry. We also show that non-negativity assumption is not crucial.

Relation to Gao et al. (2021); Xu et al. (2022). The minimalistic setting is sorely missed in Xu et al. (2022); Gao et al. (2021) and is treated only in passing in Gao et al. (2019). We consider our systematic investigation of the minimalistic setting the main contribution of our paper.

See Appendix A.1 for more related papers. Also see Section 4.4 for relation to continuous attractor neural networks.

8 Conclusion

This paper investigates the conformal isometry hypothesis as a fundamental mathematical principle for the emergence of hexagon periodic patterns of grid cells. The conformal isometry hypothesis is simple and natural, with compelling geometric implications. It is a mathematical formalization of the notion that grid cells form internal maps that enable the agent to be aware of the local geometry of the 2D physical space with different metrics but without distortion. The hypothesis is also general enough that it leads to hexagon grid patterns regardless of the concrete forms of the transformation models for path integration. It is our hope that the hypothesis will serve as a foundation for further development of normative models of grid cells as well as their interactions with other systems.

References

- Haggai Agmon and Yoram Burak. A theory of joint attractor dynamics in the hippocampus and the entorhinal cortex accounts for artificial remapping and grid cell field-to-field variability. *eLife*, 9: e56894, 2020.
- Daniel J Amit. *Modeling brain function: The world of attractor neural networks*. Cambridge university press, 1992.

- Neil W Ashcroft, N David Mermin, et al. Solid state physics, 1976.
- Andrea Banino, Caswell Barry, Benigno Uribe, Charles Blundell, Timothy Lillicrap, Piotr Mirowski, Alexander Pritzel, Martin J Chadwick, Thomas Degris, and Joseph Modayil. Vector-based navigation using grid-like representations in artificial agents. *Nature*, 557(7705):429, 2018.
- Caswell Barry, Robin Hayman, Neil Burgess, and Kathryn J Jeffery. Experience-dependent rescaling of entorhinal grids. *Nature neuroscience*, 10(6):682–684, 2007.
- Jacob LS Bellmund, Peter Gärdenfors, Edvard I Moser, and Christian F Doeller. Navigating cognition: Spatial codes for human thinking. *Science*, 362(6415):eaat6766, 2018.
- Hugh T Blair, Adam C Welday, and Kechen Zhang. Scale-invariant memory representations emerge from moire interference between grid fields that produce theta oscillations: a computational model. *Journal of Neuroscience*, 27(12):3211–3229, 2007.
- Charlotte N Boccara, Michele Nardin, Federico Stella, Joseph O’Neill, and Jozsef Csicsvari. The entorhinal cognitive map is attracted to goals. *Science*, 363(6434):1443–1447, 2019.
- Yoram Burak and Ila R Fiete. Accurate path integration in continuous attractor network models of grid cells. *PLoS computational biology*, 5(2):e1000291, 2009.
- Alexandra O Constantinescu, Jill X O’Reilly, and Timothy EJ Behrens. Organizing conceptual knowledge in humans with a gridlike code. *Science*, 352(6292):1464–1468, 2016.
- Jonathan J Couey, Aree Witoelar, Sheng-Jia Zhang, Kang Zheng, Jing Ye, Benjamin Dunn, Rafal Czakowski, May-Britt Moser, Edvard I Moser, Yasser Roudi, et al. Recurrent inhibitory circuitry as a mechanism for grid formation. *Nature neuroscience*, 16(3):318–324, 2013.
- Christopher J Cueva and Xue-Xin Wei. Emergence of grid-like representations by training recurrent neural networks to perform spatial localization. *arXiv preprint arXiv:1803.07770*, 2018.
- Christopher J Cueva, Peter Y Wang, Matthew Chin, and Xue-Xin Wei. Emergence of functional and structural properties of the head direction system by optimization of recurrent neural networks. *International Conferences on Learning Representations (ICLR)*, 2020.
- Licurgo de Almeida, Marco Idiart, and John E Lisman. The input–output transformation of the hippocampal granule cells: from grid cells to place fields. *Journal of Neuroscience*, 29(23):7504–7512, 2009.
- Christian F Doeller, Caswell Barry, and Neil Burgess. Evidence for grid cells in a human memory network. *Nature*, 463(7281):657, 2010.
- Yedidyah Dordek, Daniel Soudry, Ron Meir, and Dori Derdikman. Extracting grid cell characteristics from place cell inputs using non-negative principal component analysis. *Elife*, 5:e10094, 2016.
- William Dorrell, Peter E Latham, Timothy EJ Behrens, and James CR Whittington. Actionable neural representations: Grid cells from minimal constraints. *arXiv preprint arXiv:2209.15563*, 2022.
- William Gerard Dwyer and CW Wilkerson. The elementary geometric structure of compact lie groups. *Bulletin of the London Mathematical Society*, 30(4):337–364, 1998.
- Ila R Fiete, Yoram Burak, and Ted Brookings. What grid cells convey about rat location. *Journal of Neuroscience*, 28(27):6858–6871, 2008.
- Mark C Fuhs and David S Touretzky. A spin glass model of path integration in rat medial entorhinal cortex. *Journal of Neuroscience*, 26(16):4266–4276, 2006.
- Marianne Fyhn, Sturla Molden, Menno P Witter, Edvard I Moser, and May-Britt Moser. Spatial representation in the entorhinal cortex. *Science*, 305(5688):1258–1264, 2004.
- Marianne Fyhn, Torkel Hafting, Menno P Witter, Edvard I Moser, and May-Britt Moser. Grid cells in mice. *Hippocampus*, 18(12):1230–1238, 2008.

- Ruiqi Gao, Jianwen Xie, Song-Chun Zhu, and Ying Nian Wu. Learning grid cells as vector representation of self-position coupled with matrix representation of self-motion. In *International Conference on Learning Representations*, 2019.
- Ruiqi Gao, Jianwen Xie, Xue-Xin Wei, Song-Chun Zhu, and Ying Nian Wu. On path integration of grid cells: group representation and isotropic scaling. In *Neural Information Processing Systems*, 2021.
- Richard J Gardner, Erik Hermansen, Marius Pachitariu, Yoram Burak, Nils A Baas, Benjamin J Dunn, May-Britt Moser, and Edvard I Moser. Toroidal topology of population activity in grid cells. *bioRxiv*, 2021.
- Mariana Gil, Mihai Ancau, Magdalene I Schlesiger, Angela Neitz, Kevin Allen, Rodrigo J De Marco, and Hannah Monyer. Impaired path integration in mice with disrupted grid cell firing. *Nature neuroscience*, 21(1):81–91, 2018.
- Gily Ginosar, Johnatan Aljadeff, Liora Las, Dori Derdikman, and Nachum Ulanovsky. Are grid cells used for navigation? on local metrics, subjective spaces, and black holes. *Neuron*, 111(12):1858–1875, 2023.
- Torkel Hafting, Marianne Fyhn, Sturla Molden, May-Britt Moser, and Edvard I Moser. Microstructure of a spatial map in the entorhinal cortex. *Nature*, 436(7052):801, 2005.
- Aidan J Horner, James A Bisby, Ewa Zotow, Daniel Bush, and Neil Burgess. Grid-like processing of imagined navigation. *Current Biology*, 26(6):842–847, 2016.
- Joshua Jacobs, Christoph T Weidemann, Jonathan F Miller, Alec Solway, John F Burke, Xue-Xin Wei, Nanthia Suthana, Michael R Sperling, Ashwini D Sharan, Itzhak Fried, et al. Direct recordings of grid-like neuronal activity in human spatial navigation. *Nature neuroscience*, 16(9):1188, 2013.
- Nathaniel J Killian, Michael J Jutras, and Elizabeth A Buffalo. A map of visual space in the primate entorhinal cortex. *Nature*, 491(7426):761, 2012.
- Diederik P Kingma and Jimmy Ba. Adam: A method for stochastic optimization. *arXiv preprint arXiv:1412.6980*, 2014.
- Rosamund F Langston, James A Ainge, Jonathan J Couey, Cathrin B Canto, Tale L Bjerknes, Menno P Witter, Edvard I Moser, and May-Britt Moser. Development of the spatial representation system in the rat. *Science*, 328(5985):1576–1580, 2010.
- Bruce L McNaughton, Francesco P Battaglia, Ole Jensen, Edvard I Moser, and May-Britt Moser. Path integration and the neural basis of the ‘cognitive map’. *Nature Reviews Neuroscience*, 7(8):663, 2006.
- May-Britt Moser and Edvard I Moser. Where am i? where am i going? *Scientific American*, 314(1):26–33, 2016.
- Aran Nayebi, Alexander Attinger, Malcolm Campbell, Kiah Hardcastle, Isabel Low, Caitlin S Mallory, Gabriel Mel, Ben Sorscher, Alex H Williams, Surya Ganguli, et al. Explaining heterogeneity in medial entorhinal cortex with task-driven neural networks. *Advances in Neural Information Processing Systems*, 34:12167–12179, 2021.
- John O’Keefe and Jonathan Dostrovsky. The hippocampus as a spatial map: preliminary evidence from unit activity in the freely-moving rat. *Brain research*, 1971.
- John O’keefe and Lynn Nadel. Précis of o’keefe & nadel’s the hippocampus as a cognitive map. *Behavioral and Brain Sciences*, 2(4):487–494, 1979.
- Hugh Pastoll, Lukas Solanka, Mark CW van Rossum, and Matthew F Nolan. Feedback inhibition enables theta-nested gamma oscillations and grid firing fields. *Neuron*, 77(1):141–154, 2013.
- Thomas Ridler, Jonathan Witton, Keith G Phillips, Andrew D Randall, and Jonathan T Brown. Impaired speed encoding is associated with reduced grid cell periodicity in a mouse model of tauopathy. *bioRxiv*, page 595652, 2019.

- David C Rowland, Horst A Obenhaus, Emilie R Skytøen, Qiangwei Zhang, Cliff G Kentros, Edvard I Moser, and May-Britt Moser. Functional properties of stellate cells in medial entorhinal cortex layer ii. *Elife*, 7:e36664, 2018.
- Francesca Sargolini, Marianne Fyhn, Torkel Hafting, Bruce L McNaughton, Menno P Witter, May-Britt Moser, and Edvard I Moser. Conjunctive representation of position, direction, and velocity in entorhinal cortex. *Science*, 312(5774):758–762, 2006.
- Lawrence K Saul, Kilian Q Weinberger, Fei Sha, Jihun Ham, and Daniel D Lee. Spectral methods for dimensionality reduction. *Semi-supervised learning*, 3, 2006.
- Rylan Schaeffer, Mikail Khona, and Ila Fiete. No free lunch from deep learning in neuroscience: A case study through models of the entorhinal-hippocampal circuit. *Advances in Neural Information Processing Systems*, 35:16052–16067, 2022.
- Rylan Schaeffer, Mikail Khona, Tzuhsuan Ma, Cristóbal Eyzaguirre, Sanmi Koyejo, and Ila Rani Fiete. Self-supervised learning of representations for space generates multi-modular grid cells. *arXiv preprint arXiv:2311.02316*, 2023.
- Vemund Schøyen, Markus Borud Pettersen, Konstantin Holzhausen, Marianne Fyhn, Anders Malthe-Sørensen, and Mikkel Elle Lepperød. Coherently remapping toroidal cells but not grid cells are responsible for path integration in virtual agents. *bioRxiv*, pages 2022–08, 2022.
- Vemund Sigmundson Schoyen, Kosio Beshkov, Markus Borud Pettersen, Erik Hermansen, Konstantin Holzhausen, Anders Malthe-Sørensen, Marianne Fyhn, and Mikkel Elle Lepperød. Hexagons all the way down: Grid cells as a conformal isometric map of space. *bioRxiv*, pages 2024–02, 2024.
- Ben Sorscher, Gabriel Mel, Surya Ganguli, and Samuel Ocko. A unified theory for the origin of grid cells through the lens of pattern formation. *Advances in neural information processing systems*, 32, 2019.
- Ben Sorscher, Gabriel C Mel, Samuel A Ocko, Lisa M Giocomo, and Surya Ganguli. A unified theory for the computational and mechanistic origins of grid cells. *Neuron*, 111(1):121–137, 2023.
- Sameet Sreenivasan and Ila Fiete. Grid cells generate an analog error-correcting code for singularly precise neural computation. *Nature neuroscience*, 14(10):1330, 2011.
- Kimberly L Stachenfeld, Matthew M Botvinick, and Samuel J Gershman. The hippocampus as a predictive map. *Nature neuroscience*, 20(11):1643, 2017.
- Martin Stemmler, Alexander Mathis, and Andreas VM Herz. Connecting multiple spatial scales to decode the population activity of grid cells. *Science Advances*, 1(11):e1500816, 2015.
- Hanne Stensola, Tor Stensola, Trygve Solstad, Kristian Frøland, May-Britt Moser, and Edvard I Moser. The entorhinal grid map is discretized. *Nature*, 492(7427):72, 2012.
- Edward C Tolman. Cognitive maps in rats and men. *Psychological review*, 55(4):189, 1948.
- Ashish Vaswani, Noam Shazeer, Niki Parmar, Jakob Uszkoreit, Llion Jones, Aidan N Gomez, Łukasz Kaiser, and Illia Polosukhin. Attention is all you need. *Advances in neural information processing systems*, 30, 2017.
- Xue-Xin Wei, Jason Prentice, and Vijay Balasubramanian. A principle of economy predicts the functional architecture of grid cells. *Elife*, 4:e08362, 2015.
- James CR Whittington, Joseph Warren, and Timothy EJ Behrens. Relating transformers to models and neural representations of the hippocampal formation. *arXiv preprint arXiv:2112.04035*, 2021.
- Dehong Xu, Ruiqi Gao, Wen-Hao Zhang, Xue-Xin Wei, and Ying Nian Wu. Conformal isometry of lie group representation in recurrent network of grid cells. *arXiv preprint arXiv:2210.02684*, 2022.
- Michael M Yartsev, Menno P Witter, and Nachum Ulanovsky. Grid cells without theta oscillations in the entorhinal cortex of bats. *Nature*, 479(7371):103, 2011.
- Sheng-Jia Zhang, Jing Ye, Chenglin Miao, Albert Tsao, Ignas Cerniauskas, Debora Ledergerber, May-Britt Moser, and Edvard I Moser. Optogenetic dissection of entorhinal-hippocampal functional connectivity. *Science*, 340(6128), 2013.

A Appendix / supplemental material

A.1 More about related work

In computational neuroscience, hand-crafted continuous attractor neural networks (CANN) (Amit, 1992; Burak and Fiete, 2009; Couey et al., 2013; Pastoll et al., 2013; Agmon and Burak, 2020) were designed for grid cells.

In machine learning, the pioneering papers (Cueva and Wei, 2018; Banino et al., 2018) learned RNNs for grid cells. However, RNNs do not always learn hexagon grid patterns. PCA-based basis expansion models (Dordek et al., 2016; Stachenfeld et al., 2017) and some theoretical accounts based on learned RNNs (Sorscher et al., 2019, 2023) rely on non-negativity assumption and the difference of Gaussian kernels for the place cells to explain the hexagon grid pattern. (Dorrell et al., 2022) proposes an optimization-based approach to learn grid cells.

Recent work (Schaeffer et al., 2022) showed the prior works require hand-crafted and non-biological plausible readout representation.

A.2 More training details

All the models were trained on a single 2080 Ti GPU for 200,000 iterations with learning rate 0.003. For batch size, we generated 4000 simulated data for each iteration. For single module models, the training time is less than 15 minutes. For multi module models, the training time is less than 1 hour.

A.3 Isotropy of hexagon periodicity

Consider the following prototype model $v(\mathbf{x}) = \mathbf{U}e(\mathbf{x})$, where $e(\mathbf{x}) = (e^{i\langle \mathbf{a}_k, \mathbf{x} \rangle}, k = 1, \dots, d)$ is a d -dimensional vector with $d = 2$ for square and $d = 3$ for hexagon, and \mathbf{U} is a $d \times d$ unitary matrix. Such a prototype model was studied in Gao et al. (2021), which shows $v(\mathbf{x})$ satisfies the linear transformation model. We shall derive an interesting new property that distinguishes square periodicity and hexagon periodicity.

For square periodicity, $d = 2$ (which amounts to 4-dimensional vector because the components are complex numbers), and $\mathbf{a}_1 \perp \mathbf{a}_2$. For hexagon periodicity, $d = 3$ (which amounts to 6-dimensional vector), and $(\mathbf{a}_k, k = 1, 2, 3)$ forms a tight frame. Then

$$\langle v(\mathbf{x}), v(\mathbf{x} + \Delta \mathbf{x}) \rangle = \sum_{k=1}^d \cos(\langle \mathbf{a}_k, \Delta \mathbf{x} \rangle) \quad (14)$$

$$= \sum_{k=1}^d \left[1 - \frac{1}{2!} \langle \mathbf{a}_k, \Delta \mathbf{x} \rangle^2 + \frac{1}{4!} \langle \mathbf{a}_k, \Delta \mathbf{x} \rangle^4 \right] + o(\|\Delta \mathbf{x}\|^4). \quad (15)$$

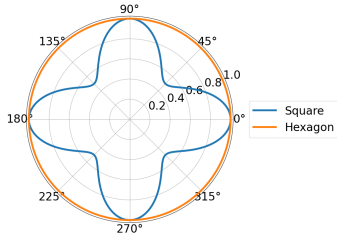


Figure 6: Isotropy.

For both square and hexagon periodicity, $\sum_k \langle \mathbf{a}_k, \Delta \mathbf{x} \rangle^2$ is isotropic, i.e., only depends on $\|\Delta \mathbf{x}\|$, and independent of the direction θ of $\Delta \mathbf{x}$. However, for $\sum_k \langle \mathbf{a}_k, \Delta \mathbf{x} \rangle^4$, it remains isotropic for hexagon periodicity, but non-isotropic for square periodicity. Figure 6 plots $\sum_k \langle \mathbf{a}_k, \Delta \mathbf{x} \rangle^4$ over direction $\theta \in [0, 2\pi]$ (with maximum normalized to 1) for square and hexagon cases.

Below is a detailed calculation. Without loss of generality, let us assume $\|\mathbf{a}_k\| = 1$. For square periodicity, we can take $\mathbf{a}_1 = (1, 0)$, $\mathbf{a}_2 = (0, 1)$. Let $\Delta \mathbf{x} = \Delta r(\cos \theta, \sin \theta)$. Then

$$\langle \mathbf{a}_1, \Delta \mathbf{x} \rangle^2 + \langle \mathbf{a}_2, \Delta \mathbf{x} \rangle^2 = \Delta r^2, \quad (16)$$

which is isotropic. But

$$\langle \mathbf{a}_1, \Delta \mathbf{x} \rangle^4 + \langle \mathbf{a}_2, \Delta \mathbf{x} \rangle^4 = \Delta r^4 (\cos^4 \theta + \sin^4 \theta), \quad (17)$$

which depends on θ .

For hexagon periodicity, we can take $\mathbf{a}_1 = (1, 0)$, $\mathbf{a}_2 = (-1/2, \sqrt{3}/2)$, and $\mathbf{a}_3 = (-1/2, -\sqrt{3}/2)$. Then

$$\langle \mathbf{a}_1, \Delta \mathbf{x} \rangle^2 + \langle \mathbf{a}_2, \Delta \mathbf{x} \rangle^2 + \langle \mathbf{a}_3, \Delta \mathbf{x} \rangle^2 = \frac{3}{2} \Delta r^2, \quad (18)$$

which is isotropic.

$$\langle \mathbf{a}_1, \Delta \mathbf{x} \rangle^4 + \langle \mathbf{a}_2, \Delta \mathbf{x} \rangle^4 + \langle \mathbf{a}_3, \Delta \mathbf{x} \rangle^4 = \frac{9}{8} \Delta r^4, \quad (19)$$

which is also isotropic.

A.4 Background on Bravais lattice

Named after Auguste Bravais (1811-1863), the theory of Bravais lattice was developed for the study of crystallography in solid state physics.

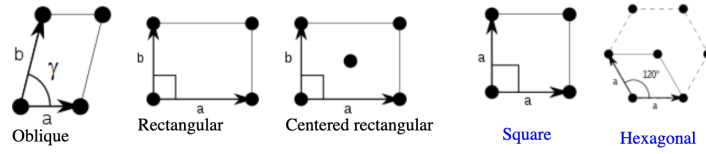


Figure 7: 2D periodic lattice is defined by two primitive vectors.

In 2D, a periodic lattice is defined by two primitive vectors $(\Delta \mathbf{x}_1, \Delta \mathbf{x}_2)$, and there are 5 different types of periodic lattices as shown in Figure 7. If $\|\Delta \mathbf{x}_1\| = \|\Delta \mathbf{x}_2\|$, then the two possible lattices are square lattice and hexagon lattice.

For Fourier analysis, we need to find the primitive vectors in the reciprocal space, $(\mathbf{a}_1, \mathbf{a}_2)$, via the relation: $\langle \mathbf{a}_i, \Delta \mathbf{x}_j \rangle = 2\pi \delta_{ij}$, where $\delta_{ij} = 1$ if $i = j$, and $\delta_{ij} = 0$ otherwise.

For a 2D periodic function $f(\mathbf{x})$ on a lattice whose primitive vectors are $(\mathbf{a}_1, \mathbf{a}_2)$ in the reciprocal space, define $\omega_k = k_1 \mathbf{a}_1 + k_2 \mathbf{a}_2$, where $k = (k_1, k_2)$ are a pair of integers (positive, negative, and zero), the Fourier expansion is $f(\mathbf{x}) = \sum_k \hat{f}(\omega_k) e^{i\langle \omega_k, \mathbf{x} \rangle}$.

A.5 Conformal modulation

For the linear model $\mathbf{v}(\mathbf{x} + \Delta \mathbf{x}) = \mathbf{v}(\mathbf{x}) + \mathbf{B}(\theta) \mathbf{v}(\mathbf{x}) \Delta r$, the directional derivative is $f(\mathbf{v}, \theta) = \mathbf{B}(\theta) \mathbf{v}(\mathbf{x})$. The conformal normalization is

$$\overline{\Delta r} = \frac{s \Delta r}{\|\mathbf{B}(\theta) \mathbf{v}(\mathbf{x})\|}. \quad (20)$$

The linear transformation model then becomes

$$\mathbf{v}(\mathbf{x} + \Delta \mathbf{x}) = \mathbf{v}(\mathbf{x}) + s \frac{\mathbf{B}(\theta) \mathbf{v}(\mathbf{x})}{\|\mathbf{B}(\theta) \mathbf{v}(\mathbf{x})\|} \Delta r. \quad (21)$$

The above model is similar to the “add + layer norm” operations in the Transformer model (Vaswani et al., 2017).

For the nonlinear model $\mathbf{v}(\mathbf{x} + \Delta \mathbf{x}) = R(\mathbf{A} \mathbf{v}(\mathbf{x}) + \mathbf{B}(\theta) \mathbf{v}(\mathbf{x}) \Delta r + \mathbf{b})$, where \mathbf{A} is a learnable matrix, and $R(\cdot)$ is elementwise nonlinear rectification, the directional derivative is $f(\mathbf{v}, \theta) = R'(\mathbf{A} \mathbf{v}) \odot \mathbf{B}(\theta) \mathbf{v}$, where $R'(\cdot)$ is calculated elementwise, and \odot is elementwise multiplication. The conformal normalization then follows the definition.

While the linear model is defined for $\mathbf{v}(\mathbf{x})$ on the manifold M , the nonlinear model further constrains $\mathbf{v}(\mathbf{x}) = R(\mathbf{A} \mathbf{v}(\mathbf{x}))$ for $\mathbf{v}(\mathbf{x}) \in M$, where $\Delta r = 0$. If $R(\mathbf{A} \mathbf{v})$ is furthermore a contraction for \mathbf{v} that are off M , then M consists of the attractors of $R(\mathbf{A} \mathbf{v})$ for \mathbf{v} around M . The nonlinear model then becomes a continuous attractor neural network (CANN) (Amit, 1992; Burak and Fiete, 2009; Couey et al., 2013; Pastoll et al., 2013; Agmon and Burak, 2020).

A.6 Eigen analysis of transformation

For the general transformation, $v(\mathbf{x} + \Delta\mathbf{x}) = F(v(\mathbf{x}), \Delta\mathbf{x})$, we have

$$v(\mathbf{x}) = F(v(\mathbf{x}), 0), \quad (22)$$

$$v(\mathbf{x} + \Delta\mathbf{x}) = F(v(\mathbf{x} + \Delta\mathbf{x}), 0), \quad (23)$$

thus

$$\Delta v = v(\mathbf{x} + \Delta\mathbf{x}) - v(\mathbf{x}) = F'_v(v(\mathbf{x}))\Delta v + o(\|\Delta v\|), \quad (24)$$

where

$$F'_v(v) = \frac{\partial}{\partial \Delta} F(v + \Delta, 0) |_{\Delta=0}. \quad (25)$$

Thus Δv is in the 2D eigen subspace of $F'_v(v(\mathbf{x}))$ with eigenvalue 1.

At the same time,

$$v(\mathbf{x} + \Delta\mathbf{x}) = F(v(\mathbf{x}), \Delta\mathbf{x}) = v(\mathbf{x}) + F'_{\Delta\mathbf{x}}(v(\mathbf{x}))\Delta\mathbf{x}, \quad (26)$$

where

$$F'_{\Delta\mathbf{x}}(v) = \frac{\partial}{\partial \Delta\mathbf{x}} F(v, \Delta\mathbf{x}) |_{\Delta\mathbf{x}=0}. \quad (27)$$

Thus

$$\Delta v = F'_{\Delta\mathbf{x}}(v(\mathbf{x}))\Delta\mathbf{x}, \quad (28)$$

that is, the two columns of $F'_{\Delta\mathbf{x}}(v(\mathbf{x}))$ are the two vectors that span the eigen subspace of $F'_v(v(\mathbf{x}))$ with eigenvalue 1. If we further assume conformal isometry, then the two column vectors of $F'_{\Delta\mathbf{x}}(v(\mathbf{x}))$ are orthogonal and of equal length, so that Δv is conformal to $\Delta\mathbf{x}$.

The above analysis is about $v(\mathbf{x})$ on the manifold. We want the remaining eigenvalues of $F'_v(v(\mathbf{x}))$ to be less than 1, so that, off the manifold, $F(v, 0)$ will bring v closer to the manifold, i.e., the manifold consists of attractor points of F , and F is an attractor network.

A.7 More experiment results on multi-module setting

A.7.1 Learned patterns

In Figures 8 and 9, we show the learned grid patterns from the linear and nonlinear models with conformal modulation. For the nonlinear model, we experimented with different rectification functions, including GELU and Tanh. As depicted in Figure 9, hexagonal grid firing patterns can emerge using diverse activation functions.

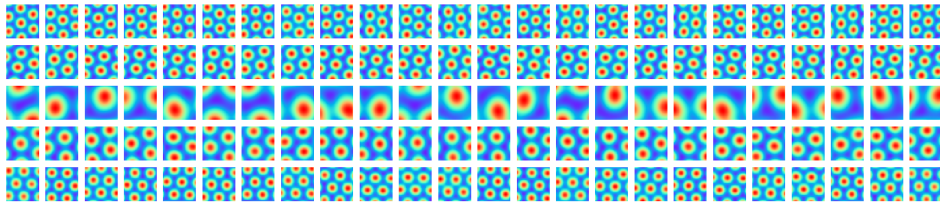


Figure 8: In the linear model, hexagon grid firing patterns are observed in the learned $v(\mathbf{x})$. Each row displays the firing patterns of all the cells within a single module, with each module comprising 24 cells. The units illustrate the neuron activity throughout the entire 2D square environment. The figure presents patterns from five randomly chosen modules.

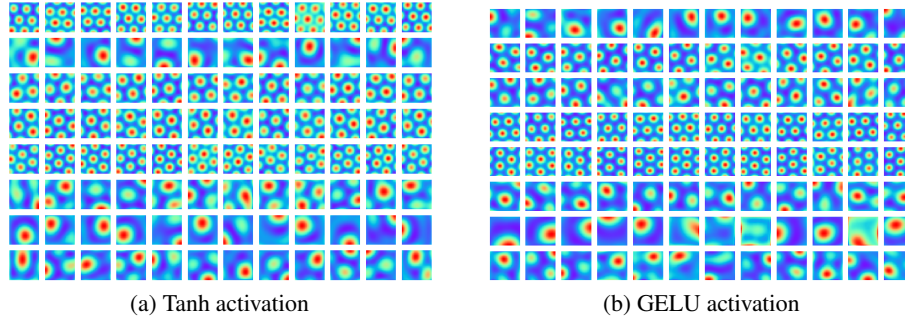


Figure 9: Results of the non-linear models. We randomly chose 8 modules and showed the firing patterns with different rectification functions.

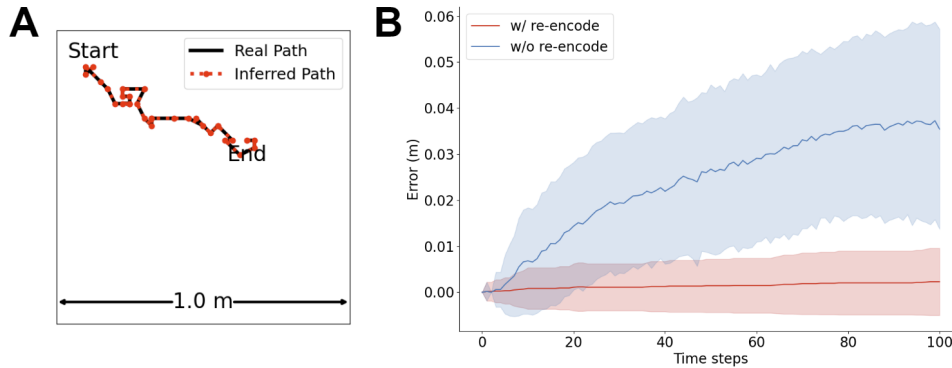


Figure 10: Results for path integration. (A) Path integration for 30 steps without re-encoding. The black line represents the real trajectory and the red one is the predicted trajectory by the learned model. (B) Results for long-distance (100-step) path integration error with and without re-encoding over time by the non-linear model.

A.7.2 Path integration

Suppose the agent starts from \mathbf{x}_0 , with vector representation $\mathbf{v}_0 = \mathbf{v}(\mathbf{x}_0)$. If the agent makes a sequence of moves $(\Delta \mathbf{x}_t, t = 1, \dots, T)$, then the vector \mathbf{v} is updated by $\mathbf{v}_t = F(\mathbf{v}_{t-1}, \Delta \mathbf{x}_t)$. At time t , the self-position of the agent can be decoded by $\hat{\mathbf{x}} = \arg \max_{\mathbf{x}'} \langle \mathbf{v}_t, \mathbf{w}(\mathbf{x}') \rangle$, i.e., the place \mathbf{x}' that is the most adjacent to the self-position represented by \mathbf{v}_t . This enables the agent to infer and keep track of its position based on its self-motion even in darkness.

We assess the ability of the learned model to execute accurate path integration in two different scenarios. First of all, for path integration with re-encoding, we decode $\mathbf{v} \rightarrow \hat{\mathbf{x}}$ to the 2D physical space via $\hat{\mathbf{x}} = \arg \max_{\mathbf{x}'} \langle \mathbf{v}, \mathbf{u}(\mathbf{x}') \rangle$, and then encode $\mathbf{v} \leftarrow \mathbf{v}(\hat{\mathbf{x}})$ back to the neuron space intermittently. This approach aids in rectifying the errors accumulated in the neural space throughout the transformation. Conversely, in scenarios excluding re-encoding, the transformation is applied exclusively using the neuron vector \mathbf{v} . In Figure 10(A), the model adeptly handles path integration up to 30 steps (short distance) without the need for re-encoding. The figure illustrates trajectories with a fixed step size of three grids, enhancing the visibility of discrepancies between predicted and actual paths. It is important to note that the physical space was not discretized in our experiments, allowing the agent to choose any step size flexibly. For path integration with longer distances, we evaluate the learned model for 100 steps over 300 trajectories. As shown in Figure 10(B), with re-encoding, the path integration error for the last step is as small as 0.003, while the average error over the 100-step trajectory is 0.002. Without re-encoding, the error is relatively larger, where the average error over the entire trajectory is approximately 0.024, and it reaches 0.037 for the last step.